ORIGINAL RESEARCH ARTICLE

Effect of Holding Time on Populations of Microparticles in Spheroidal Graphite Irons

L. MICHELS, A.J.F. PIRES, C.A.S. RIBEIRO, B. KROKA, E.G. HOEL, E. OTT, and C. HARTUNG

Non-metallic microparticles in spheroidal graphite irons are a product of the inoculation and the Mg-treatment of the liquid melt. Besides the influence on the mechanical properties of these iron–carbon–silicon alloys, they are also responsible for the nucleation and the morphology of the graphite phase. The present investigation is undertaken to study holding time effects of a (Ba, Ca, Al)–ferrosilicon (called Ba-inoculant) and (Ca, Al)–ferrosilicon (called Ca-inoculant) inoculants on the overall distribution of microparticles. Using the 2D to 3D conversions method, which is typically used for graphite nodules, the non-metallic microparticles' statistical parameters, such as size distributions and number densities, are quantified. The total number of particles is similar after Mg-treatment and inoculation for Ca-inoculant but not for Ba-inoculated samples, which lose approximately 25 pct of microparticles after 1 minute of holding time. Iron treated with the Ca-inoculant loses about 37 pct of its nodules after 5 minutes, while the Ba-inoculated melts maintain their performance even after 10 minutes. Based on extrapolating the trend of the undercooling, Ba-inoculated samples would reach the uninoculated undercooling values in 48 minutes, while Ca-inoculated samples in only 11 minutes. By evaluating the size distributions of the non-metallic microparticles, the Ostwald ripening hypothesis or particle aggregation can be verified. The results suggest that sulfides are more critical for graphite nucleation since they can be correlated with the graphite number densities. However, due to the small difference in the microparticle population of the uninoculated sample with Ca-inoculated samples, other aspects of the fading mechanism need to be considered, such as transient metastable states, since the central hypothesis of loss of inclusions cannot alone explain the decrease in the nucleation frequency of graphite.

© The Author(s) 2022

L. MICHELS is with the Innovation Department, Elkem Silicon Products (ESP), Fiskåveien 100, 4621 Kristiansand, Norway and also with the Department of Physics, Norwegian University of Science and Technology (NTNU), Høgskoleringen 5, 7491 Trondheim, Norway. Contact e-mails: leander.michels@elkem.com, leander.michels@ntnu.no. A.J.F. PIRES and C.A.S. RIBEIRO are with the Departamento de Engenharia Metalúrgica e de Materiais, Faculdade de Engenharia, Universidade do Porto (FEUP), Rua Dr. Roberto Frias s/n, 4200-465 Porto, Portugal and also with the LAETA/INEGI-Institute of Science and Innovation in Mechanical and Industrial Engineering, R. Dr. Roberto Frias, 4200-465 Porto, Portugal. B. KROKA is with the Elkem Technology, Elkem ASA, Fiskåveien 100, 4621 Kristiansand, Norway. E.G. HOEL, E. OTT, and C. HARTUNG are with the Innovation Department, Elkem Silicon Products (ESP).

I. INTRODUCTION

SPHEROIDAL graphite iron (SGI) are iron–silicon–carbon alloys with several applications in society, especially in the wind energy and the automotive sectors.[1] This material can either solidify in a divorced stable eutectic reaction, in which the carbon phase nucleates and grows as graphite in spherical-shaped crystals called nodules, or as a metastable phase, iron-carbide (Fe_3C) or as a mix of both. In the applications mentioned above, the desired state of carbon is the graphite phase from the divorced eutectic reaction. Stable to metastable transition depends on the composition, cooling rate, and melt treatments.[2] The presence of silicon changes the solidification behavior of SGI by shifting the temperatures of the eutectic and eutectoid transformations.[3] Usually, to avoid metastable solidification, it is necessary to treat the melt with additives, such as ferrosilicon-based inoculants and nodularizers.[4]

The effect of inoculation in cast iron is widely discussed in the literature.[5–9] For SGI, its purpose is to increase nodule count, prevent carbides and shrinkage formation. Inoculants are usually X–ferrosilicon, where X can be a combination of several elements but mainly contains Ca, Sr, Ba, Ce, Al, and Zr.[8,10] It has been demonstrated that the dissolution of these alloys will promote the formation of microparticles, such as sulfides, oxides, nitrides, and carbides, which can later act as nucleation sites for graphite to grow.[5] Most of the studies in SGI are devoted to (i) the structure of a few of these microparticles and their interface with graphite,[11–14] (ii) their composition,[6,14,15] or (iii) the aspect of graphite growth, such as kinetics and morphology.[16–21] However, very few are dedicated to studying morphology, size distributions, and the total number densities of these non-metallic microparticles.

Therefore, the present manuscript investigates the effects of inoculation and holding time on the graphite and microparticle populations. It is said in the industry that the inoculant effect fades with time, for example, when holding inoculated melt in a pouring vessel before casting. In the case of SGI, fading is generally described as a loss of graphite nodule count density or/and deterioration of the graphite morphology.[22–24] The mechanism often mentioned to explain this observation is the Ostwald ripening,[4,25,26] a diffusion-controlled process that causes the growth of larger particles at the expense of smaller ones.[27,28] However, particle aggregation resulting in a reduction in the particle number density, as observed in other types of suspensions, could also be an explanation.[28,29] Another mechanism could be the transition in the microparticles from metastable to stable phases, as proposed by Qing et al.[14]

Furthermore, it is reported that inoculants containing Ba are more fade-resistant.[10,24,30] However, studies quantifying the effect of holding time on these systems are limited. The present investigation is undertaken to study the time effect of Ba-containing inoculant and a common Ca–ferrosilicon inoculant through changes in microstructure, graphite nodule's nuclei, and non-metallic microparticles. This study uses the conversion methods from 2D to 3D as described in References 31 and 32 to study size distributions and the total number densities for graphite and the entire non-metallic microparticle population. To the best of our knowledge, this is the first time a detailed study of microparticles as a function of holding time is done for SGI.

II. METHODS

A. Alloys

SGI samples, with an average carbon content of 3.7 pct in this study, have been nodularized with Mg–FeSi and inoculated with a (Ba, Ca, Al) and a (Ca, Al) containing ferrosilicon. The compositions of the alloys are shown in Table I.

B. Samples

The experimental melt was produced in a 275 kg induction furnace from 100 pct low alloyed cast iron returns. Alloying element corrections were made through additions of high purity graphite (99.9 pct C), FeMn (75 pct Mn), and copper metal (99 pct Cu) at the furnace. The melt was tapped at 1500 °C from the furnace into a ladle containing 1.15 wt pct of an Mg–FeSi alloy with the composition shown in Table I. After the Mg–FeSi treatment, the liquid was then poured into six different alumina crucibles containing 0.3 wt pct inoculants so that each crucible contained 32 kg of iron. The liquid iron was then held for 1, 5, and 10 minutes. After the holding time, a quenched sample (known as chill coins) was collected for chemical analysis, and the remaining liquid was poured into vertical tensile bars (cylinders of 30 mm diameter) and into open thermal analysis cups (36 × 36 × 40 mm). The samples are labeled as follows: Ba-1, Ba-5, and Ba-10 are inoculated with Ba, Ca, Al–FeSi and hold for 1, 5, and 10 minutes, respectively. While Ca-1, Ca-5, and Ca-10 are samples inoculated with Ca, Al–FeSi with holding times of 1, 5, and 10 minutes, respectively. The uninoculated sample is labeled as UN. For metallographic examinations, the bars were cut at the center and etched in 2 pct Nital acid for 15 seconds.

The crucibles contained a thermocouple to measure the temperature of the liquid before pouring into the tensile bar molds and thermal analysis cups, which were recorded to be 1339, 1326, and 1313 °C for Ca-1, 5, and 10, respectively, and 1331, 1321, and 1310 °C for Ba-1, 5, and 10, respectively.

C. Chemical Characterization

The chill coins were taken into an arc spark optical emission spectrometer, and thereafter part of them was cut and evaluated with combustion techniques for pct C and pct S. The compositions of the samples are shown in Table II.

D. Thermal Analysis

Thermal analysis measurements were made by pouring liquid iron into sand crucibles with 36 × 36 × 40 mm dimensions containing a type-k thermocouple in its geometrical center. Each cup was connected to a data logger that measures temperature with a frequency of 10 Hz. The cooling curves were subsequently evaluated using a MATLAB script.

E. Microstructure

The samples' microstructure was evaluated using a Zeiss Axioplan 2 optical microscope, equipped with a Märzhäuser automatic stage controller at a magnification of 100 times. Nodule count density (nodule size cutoff < 5 μm) and ferrite/pearlite quantifications were performed on an area of 14.2 mm^2 by systematic random sampling using a Micropublisher 5.0 RTV digital camera from QImaging. The image resolution is

Table I. Composition of the Mg–Ferrosilicon and Inoculants Used

Alloy	Pct Si	Pct Ca	Pct Al	Pct Ba	Pct Mg	Pct Ce
Mg–Ferrosilicon	45.8	1.5	0.7	—	5.9	0.17
Ca, Al–Ferrosilicon	76.0	1.2	1.4	—	—	—
Ba, Ca, Al–Ferrosilicon	73.1	1.4	1.5	2.6	—	—

The balance is Fe. Carbon and oxygen content in these alloys is below 0.05 and 0.2 wt pct, respectively.

Table II. Chemical Composition of the Samples

Sample	Pct C*	Pct Si	Pct Mg	Pct Al	Pct S*	Pct Ce
UN	3.79	2.39	0.048	0.008	0.010	0.0051
Ca-1	3.71	2.62	0.045	0.011	0.013	0.0049
Ca-5	3.76	2.61	0.045	0.010	0.020	0.0044
Ca-10	3.71	2.61	0.044	0.011	0.015	0.0039
Ba-1	3.71	2.65	0.044	0.010	0.008	0.0047
Ba-5	3.72	2.61	0.044	0.010	0.008	0.0045
Ba-10	3.67	2.63	0.044	0.010	0.008	0.0043

The elements with (*) were obtained using combustion techniques. Since the melt comes from the same treatment ladle the overall composition is Mn 0.17 pct, P 0.030 pct, Ti 0.011 pct, V 0.0033 pct, Nb 0.003 pct and La 0.0012 pct. The carbon equivalent (CE) is approximately 4.50, which is calculated using CE = pct C + 0.31·pct Si + 0.33· pct P − 0.029· pct Mn + 0.41· pct S[33]

0.68 μm/pixel (1.47 pixel/μm) and an image size of 1280 × 960 pixels. The analysis is based on ASTM E2567-16a. The metallographic images for each sample are shown in Figure 1.

F. *Automated Mineral Identification and Characterization System (AMICS)*

After the microstructure quantification, the specimens were taken in an SEM to be evaluated with the AMICS software that utilizes an SEM Zeiss Merlin Compact Bruker XFlash 6130 EDX detector combined with the BSE detector signal for the determination of chemical composition, phase composition, and particle size distribution. The minimum particle area measured was 0.5 μm^2. Below this value, the particle size and composition uncertainty is large and therefore not reported. The total evaluated area is 6.27 mm^2 for all samples.

G. *Particle Count and Size Distribution*

To better quantify the difference in particle count, all the non-metallic microparticles and graphite particles were converted from 2D to 3D number densities. Several methods described in the literature can be used for this procedure.[31,34] Here, the Finite Difference Method is employed[32] to estimate the total number of particles per mm^3 and size distributions in the samples. A summary of this method is given below.

Like in the Saltykov method, the 2D size distribution is divided into k class intervals of size Δ. In this case, $(N_A)_i$ is the number of particles per unit of area (mm^{-2}) in the size interval $(i-1)\Delta$ to $i\Delta$, where $1 \leq i \leq k$. Then, $N_V(j)$ can be obtained as:

$$N_V(j) = \Delta^{-1} \sum_{i=j}^{k} \alpha(i, j) N_A(i),$$ [1]

where $\alpha(i, j)$ coefficients, according to Reference 32, can be calculated as:

$$\alpha(j, j) = \begin{cases} 1 & (i = j), \\ \frac{2}{\pi} \ln\left[\frac{j + \sqrt{j^2 - (j-1)^2}}{j-1}\right] & \forall (j > 1), \end{cases}$$ [2]

with $\alpha(i, j)$ being:

$$\alpha(i, j) = \frac{2}{\pi} \ln\left[\frac{i + \sqrt{i^2 - (j-1)^2}}{i + \sqrt{i^2 - j^2}} \cdot \frac{i - 1 + \sqrt{(i-1)^2 - j^2}}{i - 1 + \sqrt{(i-1)^2 - (j-1)^2}}\right] \quad \forall (i > j).$$ [3]

Therefore, the total number of particles in a volume is:

$$N_{V-Total} = \sum_{j=1}^{k} N_V(j\Delta).$$ [4]

III. RESULTS

A. *Metallography*

In Figure 1, the microstructure variables for SGI were quantified, specifically the nodule count density, nodularity, and matrix ratio (ferrite + pearlite = 100 pct). The results are shown in Figure 2.

Figure 2(a) shows the number of nodules per mm^2, often used to quantify casting quality in SGI. Figure 2(b) shows the nodularity, a measure of the roundness of the graphite nodules, that is indirectly related to the oxygen and sulfur activity in the melt. Figure 2(c) quantifies the ferrite content, which could not be done for the UN sample due to the presence of Fe$_3$C, see Figure 1(a). The sample with the lowest nodule count is the UN with 92 mm^{-2} with some Fe$_3$C, demonstrating the need for inoculation for this system. The highest number in nodule count, nodularity, and ferrite content was achieved with the Ca-1 sample. The fading effect is evident for Ca-5, which had an approximately 37 pct reduction in nodule count compared to Ca-1. However, Ba samples do not show any reduction in the number of nodules count over time. The slight increase in the nodule count for Ca-10 and Ba-10 might be related to a
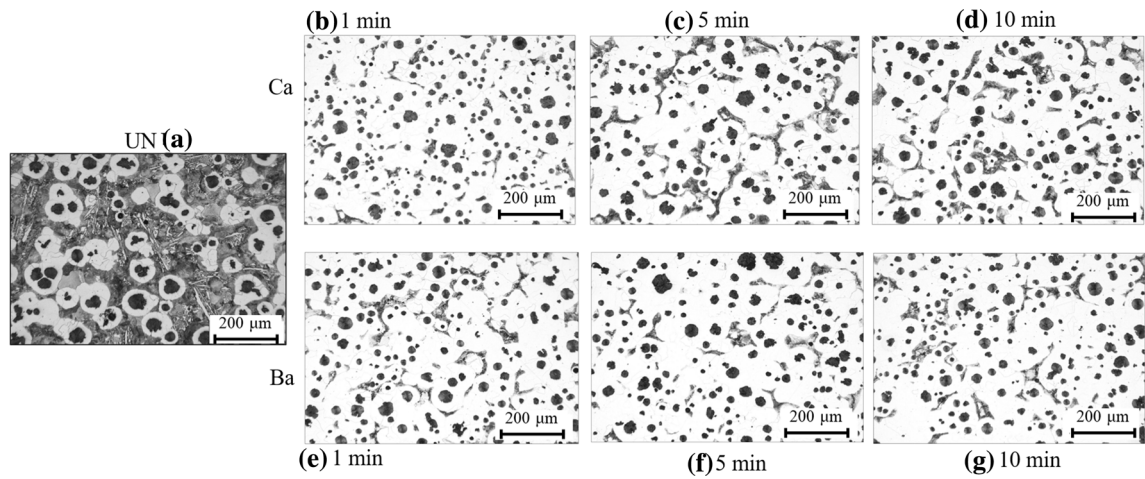
Fig. 1—Microstructure of (*a*) UN, (*b* through *d*) for Ca and (*e* through *g*) Ba samples with 1 to 10 minutes of holding time, respectively. The samples have been etched in Nital to expose the content of pearlite (gray), ferrite (white), and cementite (seen in UN).
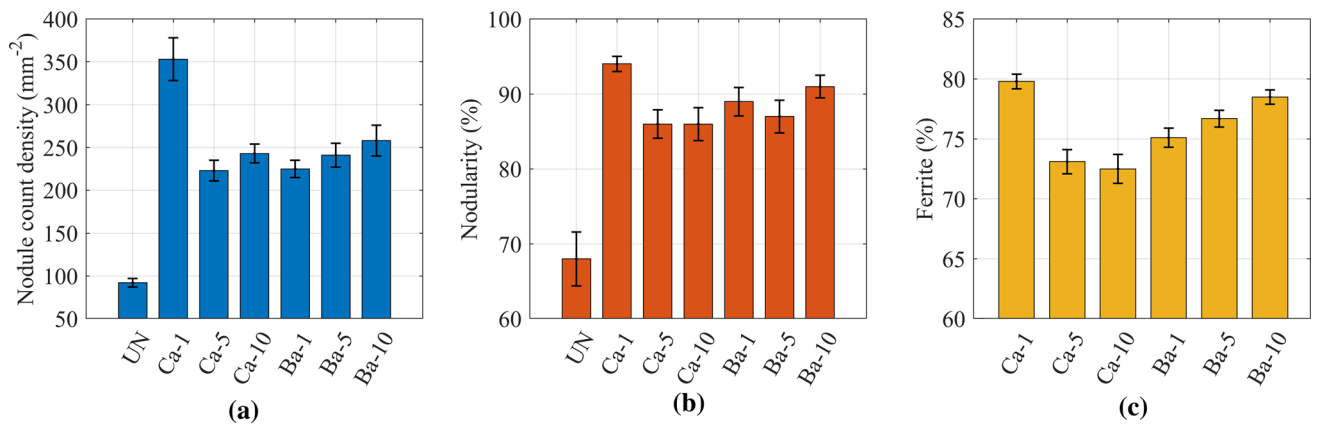

Fig. 2—Microstructure variables for SGI: (*a*) nodule count density, (*b*) nodularity (roundness), and (*c*) matrix type (ferrite + pearlite = 100 pct). Since UN contains Fe_3C, the matrix phase quantification was not performed.

colder pouring temperature, which increases the cooling rate in the mold and consequently the undercooling, causing the activation of more nucleation sites.

B. *Thermal Analysis*

To study the nucleation state of the liquid, as a function of the holding time for each sample, cooling curves from thermal analysis cups (described in the "Method" section) were recorded, and the main solidification parameters were obtained. These parameters are the low eutectic temperature (LET), high eutectic temperature (HET), recalescence (R = HET − LET), and solidus temperature (TS). A detailed description of TA curves in cast iron can be found in References 35 through 37. Figure 3 shows the cooling curves for the samples Ca and Ba, and Table III shows the obtained parameters.

In Figure 3, the main feature of the cooling curves is marked with the symbols ◇, ▽, □. They are the LET, HET, and TS, respectively. LET is related to the nucleation status of the melt. Higher LET values mean

lower undercooling, indicating a better-nucleated iron with a low tendency to form Fe_3C. This means that Ca-1 is the best immediate nucleated sample. For Ca-5 and Ca-10, a significant decrease in LET is measured. Although a reduction in LET is also observed for Ba samples, this decrease is significantly smaller when compared with Ca samples. All the samples showed an increase in R with holding time. R is related to the latent heat release during growth in the early stage of solidification. The increase of R with the holding time may be related to the reduced nucleation potential of the melt. Ba-10 has the highest R, which is related to the non-continuous precipitation/growth of graphite. This could be due to a loss of inclusions (graphite nuclei) by adding barium into the melt compared to other samples.

In order to compare the fading rates, the cooling curves were aligned so that t = 0 seconds at LET and the LET were plotted as a function of time. The results are shown in Figure 4.
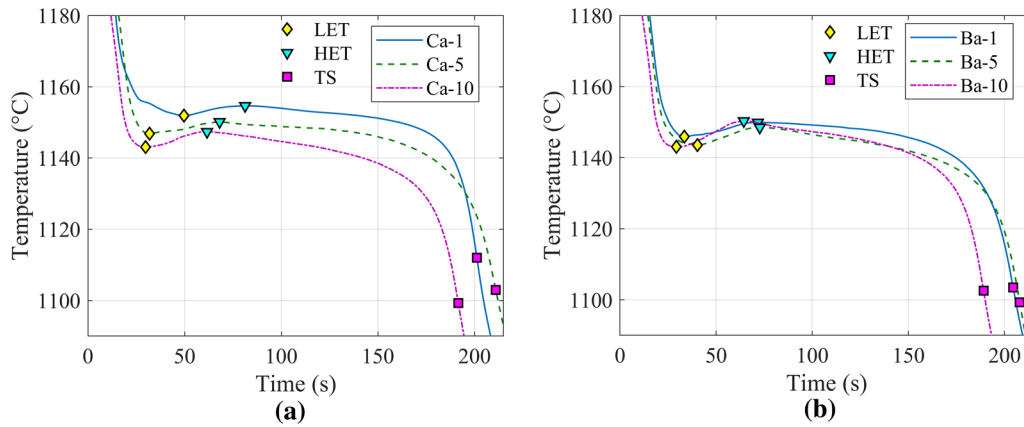
Fig. 3—Cooling curve for (a) Ca samples, and (b) Ba samples.

Table III. Thermal Analysis Parameters

Parameter	UN	Ca-1	Ca-5	Ca-10	Ba-1	Ba-5	Ba-10
LET (°C)	1141.3	1151.9	1146.8	1143.1	1145.9	1143.5	1143.0
R (°C)	4.6	3.1	3.2	3.9	4.0	4.4	6.1
TS (°C)	1086.2	1112.0	1103.0	1099.3	1103.5	1099.4	1102.61
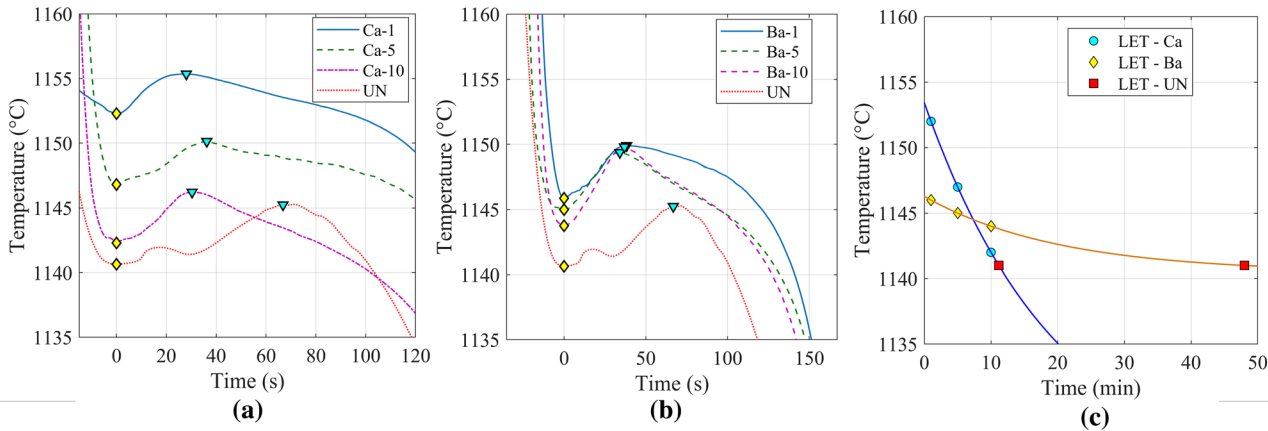
Fig. 4—(a) Cooling curves for Ca-inoculated samples, (b) Ba-inoculated samples, and (c) low eutectic temperatures (LET) values, obtained from the thermal analysis, showing a decrease as a function of time. The lines indicate an exponential decay model to estimate the fading behavior.

Figures 4(a) and (b) shows that when the cooling curves are aligned with LET at $t = 0$ seconds, the fading effect becomes explicit. Also, by plotting the LET values, see Figure 4(c), as a function of time, one can estimate the time for the nucleation level of the melt to reach the UN value and causes Fe_3C precipitation.

Using the LET value from the UN sample as a reference, the fading rate can be determined by fitting the LET as a function of time with an exponential decay:

$$\text{LET}(t) = A \cdot \exp\left(-\frac{t}{\tau}\right) + T_o, \qquad [5]$$

where A, τ and T_o are constants. Table IV shows the fitting results.

For $t = 0$ minutes, the sum of A and T_o will give the maximum LET. Using Eq. [5], the result shows that Ca-inoculated samples will reach the UN LET value in 11 minutes, while Ba-inoculated samples would take 48

minutes. The size and geometry of the casting as well as the pouring temperature, can significantly influence this parameter by changing the cooling rate.

C. SEM/AMICS

The results from microstructure and thermal analysis showed fading of the inoculation effect. These samples formed a basis for an in-depth study using the SEM/EDX with AMICS, where mapping and classification of graphite nodules, nuclei, and inclusions can be made. An example of the method is shown in Figure 5.

Based on the EDX spectra, the microparticle types were separated into four categories: sulfides, oxides, nitrides, and carbides. Clusters, as seen in Figure 5(d), are counted as separate particles. Their main elemental composition is given in Table V.

In the sulfide category, the main microparticle measured is an (Mg, Ca)S, described in detail in References 11, 14, 15, 38. Nitrides are the (Mg, Al, Si)N documented in References 12 through 14, 39. Microparticles with rare earth elements[11] and phosphorous[4] have

been counted as oxides. Barium was not detected during these measurements due to its small addition rate. The morphology and size of graphite particles can be seen in Figure 6. Note that the morphology of the graphite particles changes substantially with increasing holding time. A mechanism for this process might be related to the oxygen activity, as shown by Reference 40.

The samples chosen for this study were UN, Ca-1, Ca-10, Ba-1, and Ba-10. Figure 7 shows the number density of graphite and microparticles. Agglomeration or co-growth of several types of microparticles is not taken into account. Graphite particles are counted independent of their shape.

In Figure 7(a), the graphite number density reflects the trend observed in the optical microscope (see Figure 2), with Ca-1 having the highest value. The 2D number density of microparticles is similar for all samples, as seen in Figure 7(a). Figure 7(b) shows that the 3D microparticle number density difference is still small for UN and Ca samples. In contrast, the Ba-1 sample has the lowest microparticle density, which increases after 10 minutes of holding time (Ba-10).

The microparticles number densities separated by type are shown in Figure 8.

Figure 8(a) shows the area covered by graphite particles for each sample. The lowest value is seen for UN sample with ~ 9.5 pct, while the highest is observed in Ca-1 and Ba-10 with 11.4 and 11.7 pct, respectively. All inoculated samples show an increase in the area occupied by graphite particles compared to the UN sample. In Figures 8(b) and (c), the microparticles of all inoculated samples occupy a larger area than UN, specifically for sulfides, oxides, and carbides.

Table IV. Fitting Parameters from Eq. [1]

Parameter	Ca	Ba
A (°C)	29.10	5.82
τ (min)	20.08	20.08
T_o (°C)	1124.00	1140.00
LET_{max} (°C)	1153.10*	1145.82
Fading time (min)	11	48

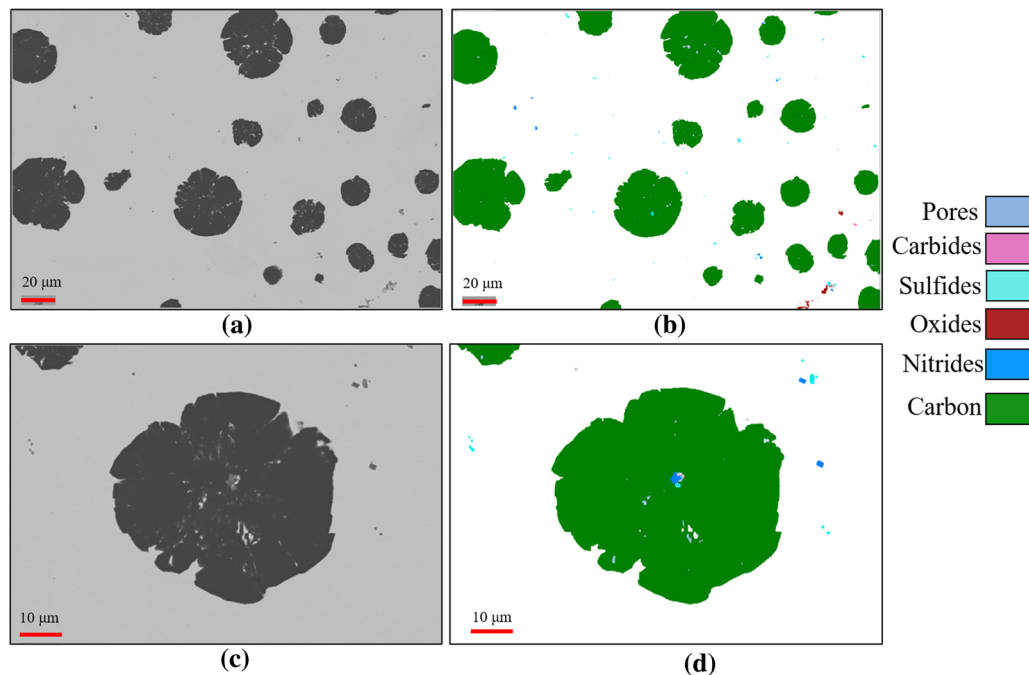*For comparison, Ca-1 LET is ~ 1152.3 °C.

Fig. 5—(a, c) SEM image of graphite nodules with microparticles around. (b, d) Image segmented and classified according to the composition of the microparticles.

Figures 8(d) and (e) shows the number density for each sample. They are divided into categories according to Table V. In the 2D number densities, graphite and oxides are the most frequent particles. After converting to 3D number densities, sulfides and oxides become the most dominant microparticles in the casting. The UN sample shows the lowest number of graphite particles and the highest oxides. The highest sulfide number is observed in Ca-1, which is substantially higher than Ca-10. In contrast, Ca-10 contains a significantly higher

oxide number density than Ca-1. These observations indicate a potential fading mechanism, where the effect of holding times can be related to a decrease in sulfides and an increase in oxides populations. In Ba-inoculated samples, Ba-10 shows an increase in the sulfides, oxides, and nitrides populations compared to Ba-1. The evolution of the density of the sulfide microparticles is the main observed difference between Ca and Ba samples: increasing holding times decreases the number density of sulfides in Ca and increases for Ba.

In order to verify the effect of holding time on graphite particles and microparticle sizes, the ferret diameter of each particle was measured and computed according to Eqs. [1] through [4]. For graphite particles, the results are shown in Figure 9.

In Figure 9, the N_v as a function of diameter was adjusted with one or more log-normal distributions[41] in the following form:

$$\frac{dn}{d\phi} = \frac{n_{max}}{\phi_\sigma \sqrt{2\pi}} \frac{1}{\phi} \exp\left[-\frac{1}{2}\left(\frac{\ln\phi - \ln\phi_o}{\phi_\sigma}\right)^2\right], \quad [6]$$

where $dn/d\phi$ is the particle density in mm^{-3}, ϕ is the diameter, n_{max} is the maximum number density, ϕ_o is the mean value, and ϕ_σ is the standard deviation. For UN sample, the size distribution curve is broad. In

Table V. Categories of Microparticles Found in the Samples

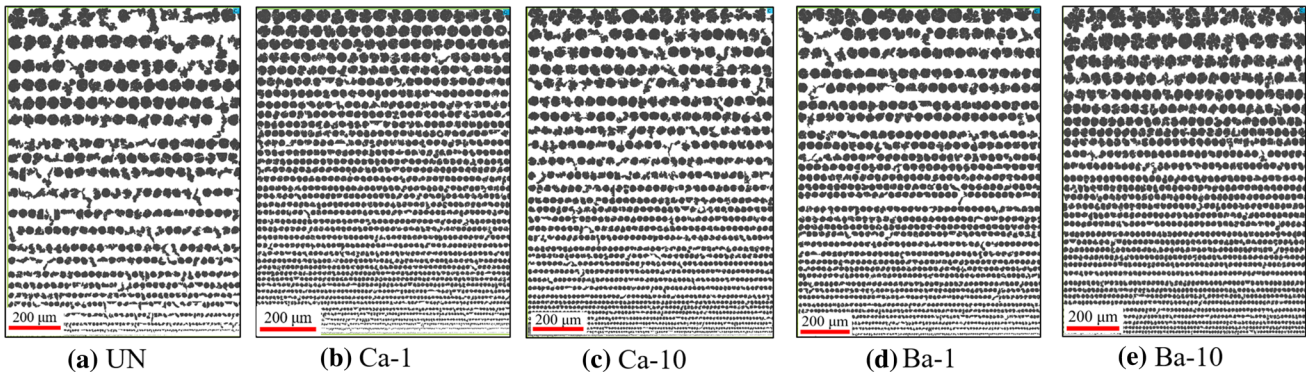| Type	Elemental Compound
Graphite	C
Sulfides	(Mg, Ca)–S
	Mg–S
	(Ce, Mg)–S
Nitrides	(Mg, Al, Si)–N
	(Ti)–N
Oxides	(Mg)–O
	(Al, Si)–O
	(Mg)–P–O
	(Ce, La, Mg)–P–O
Carbides	(Ti–Nb–V)–C

(a) UN (b) Ca-1 (c) Ca-10 (d) Ba-1 (e) Ba-10
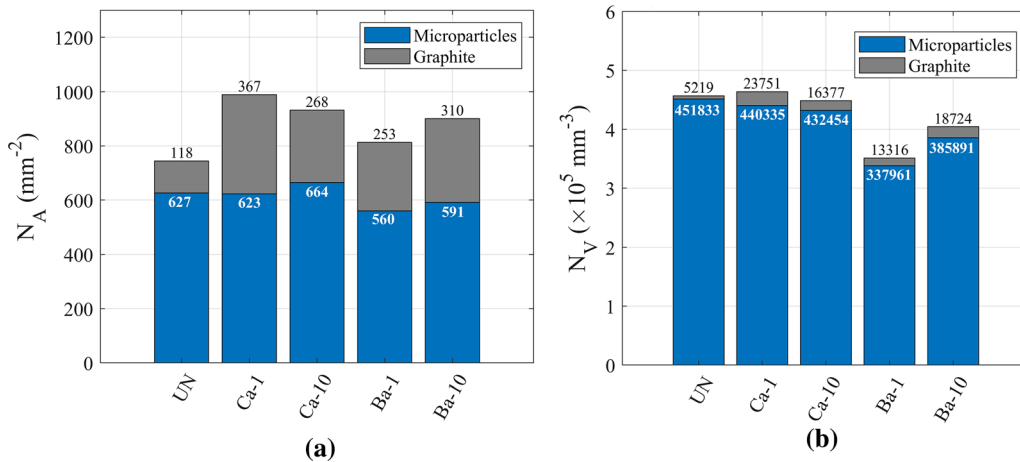
Fig. 6—The graphite morphology for each sample.

Fig. 7—(a) Microparticles and graphite particles number density per mm². (b) Number density per mm³ after the conversion using Eq. [4].
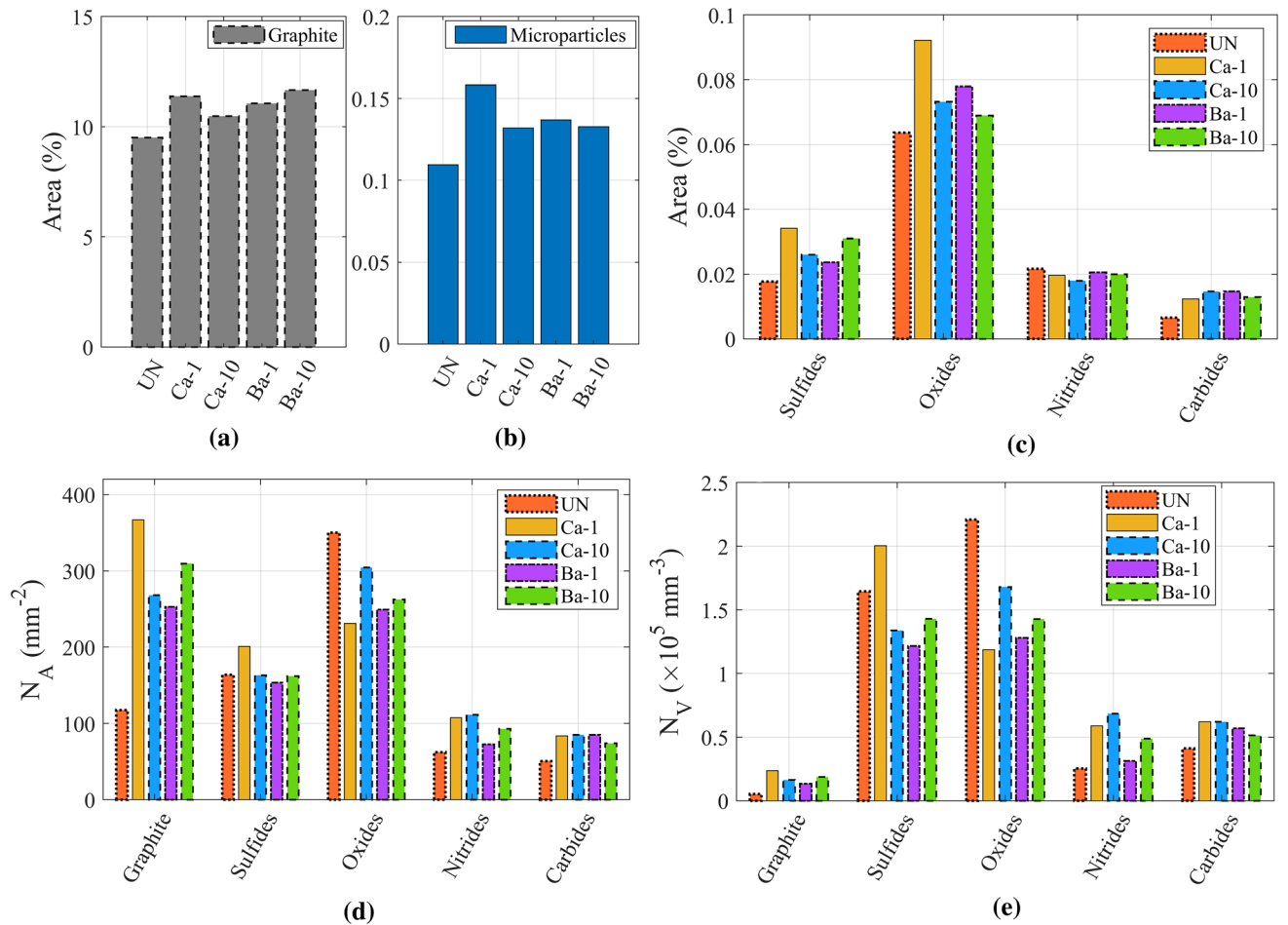
Fig. 8—(a) Area in percent cover by graphite and (b) microparticles, (c) area occupied per type of microparticle. (d) Particle number density per mm^2 and (e) per mm^3 for each sample.

contrast, the size distribution of all inoculated samples is narrower. Ca-1 is described by two log-normal functions, which are also observed in References 15, 26, and 42, and after 10 minutes of holding time, the peak at ~ 20 μm disappeared, and a peak at 46 μm appears. For Ba samples, the graphite size distribution is broader for Ba-1 than Ba-10.

The size distributions for each microparticle category are obtained by applying the same methodology to convert N_A (mm^{-2}) to N_V (mm^{-3}). The result can be seen in Figure 10.

For sulfides, in Figure 10(a), Ca-1 shows the largest peak with a center at approximately 0.7 μm. While in Ca-10, the peak shifts to ~ 1.2 μm, and the peak area decreases. This might be explained by the Ostwald ripening or particle agglomeration, causing their average size to increase. The latter phenomenon is reported to be more significant under high turbulent conditions.[29] The sulfide peak shift is not significantly observed for Ba-inoculated samples. In Figure 10(b), oxides show a distinct behavior for the UN sample, a larger and narrower size distribution. The effect of holding time can be observed in the samples Ca-1 and Ba-1 compared with Ca-10 and Ba-10. The peak area increases for the latter two, pointing to an increase in the oxide

population. Figure 10(c) shows the evolution of the particle size distributions for nitrides. A bimodal distribution is observed for the UN, Ca-1, and Ba-1 samples. With increasing holding time, the bimodal distribution seems to turn into a unimodal distribution where the peak at the highest diameters disappears, and the peak at the lowest diameters increases significantly. This effect shows that the nitrides population is affected substantially by holding time and may play a role in the fading mechanism. In the case of carbides, in Figure 10(d), no trivial differences can be observed.

IV. DISCUSSIONS

A. *Effect of Holding Time*

It is known that after inoculation, there is a time limit for its effect to fade.[22,24] Both thermal analysis and a reduction in the graphite particle count points to this phenomenon. It can be seen that Ca-inoculated samples faded faster than Ba samples. Based on the maximum undercooling, measured using thermal analysis, it was estimated that Ca-inoculated samples would reach the UN values after 11 minutes, which is similar to the
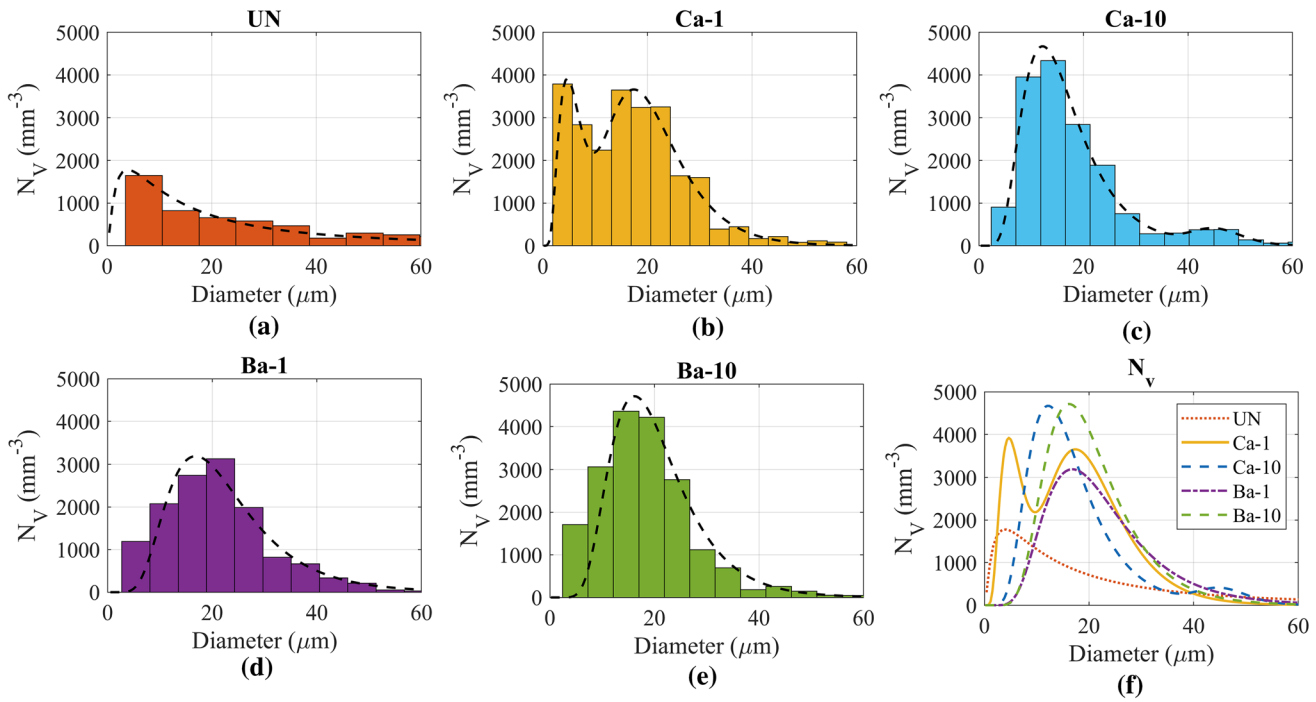
Fig. 9—(*a* through *e*) Number density in mm^{-3} as a function of particle diameter for each sample. The black lines are log-normal distributions. (*f*) The size distribution for each sample as a comparison.
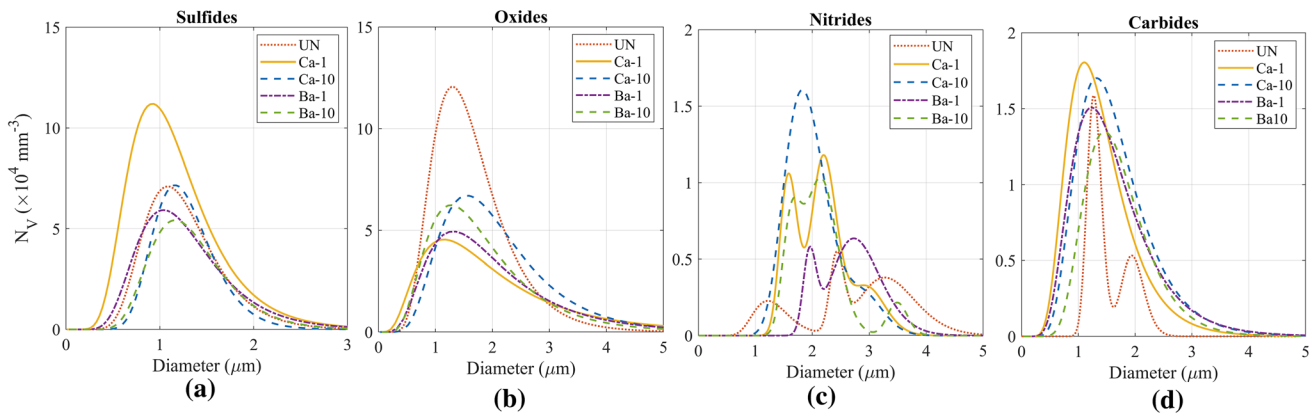

Fig. 10—Log-normal distribution of each microparticle class. (*a*) Sulfides, (*b*) Oxides, (*c*) Nitrides, and (*d*) Carbides.

results published by Fras and Górny.[22] When looking into the differences in microparticle populations, one can notice that Ca-1 has more sulfides of smaller size and fewer oxide particles than the other samples. The effect of holding time becomes explicit when looking at the results for Ca-10, where the sulfide peak in Figure 10(a) shifts to a larger size, and the peak area significantly decreases. For oxides, an increase with holding time in the peak area is observed. In both, Ca and Ba samples, the increase in the oxide population points to a re-oxidation of the liquid iron during the holding time, also suggested by Lekakh.[15] Figures 8(b) through (e) shows that inoculation with a (Ca, Al)–ferrosilicon with 1 minute holding increased the sulfide and decreased the oxide number densities, as seen in Ca-1. A similar result was reported by Qing *et al.*[14] in a combined thermodynamics and transmission electron microscope work. One can also note that nitride microparticles may play a more important role with a longer holding time since their population increases for both Ca and Ba samples. However, the present data shows that high sulfide and low oxide populations are associated with an increase in graphite particles, as seen in the relation between Ca-1 with Ca-10 and Ba-1 with Ba-10. At the same time, all inoculated samples have fewer oxide particles than UN.

B. *Nucleation Frequency*

A reasonable assumption is that all graphite nodules are nucleated heterogeneously on foreign particles, with the same chemical composition, at least in the present resolution, as the microparticles.[15] Therefore, the nucleation frequency (N_v) of the entire microparticle population can be calculated for each sample as:

$$N_{nu} = \frac{N_V^{\text{graphite}}}{N_V^{\text{graphite}} + N_V^{\text{microparticles}}} \cdot 100 \text{ pct}, \qquad [7]$$

where N_V^{graphite} is the graphite number density in mm^{-3} and $N_V^{\text{microparticles}}$ is the number density of all microparticles, both reported in Figure 7. The results are shown in Figure 11.

Figure 11 shows that only 1 pct of the microparticles are nucleating graphite for UN, while for all inoculated samples, this number is above 3 pct. The Ca-1 sample has the highest nucleation frequency with ~ 5 pct of the microparticles nucleating graphite, while after 10 minutes (Ca-10), this number decreases to ~ 3.5 pct, which is similar to Ba-1. The decrease N_v in Ca-10 (compared to Ca-1) may be attributed to a decrease in the sulfide population and an increase in the oxide population, which suggests that sulfides are more critical for graphite nucleation. An increase in the nucleation frequency is observed in the Ba-10 sample, a behavior markedly different from the Ca-10 sample. This can be associated with more microparticles since the total number density increases, particularly sulfides. It is important to note that this nucleation frequency N_v does not consider the aggregation of microparticles but the contribution of individual compositions. In general, Figure 11 shows that inoculation increases the nucleation frequency, and it demonstrates that less than 6 pct of the microparticles are nucleating graphite.
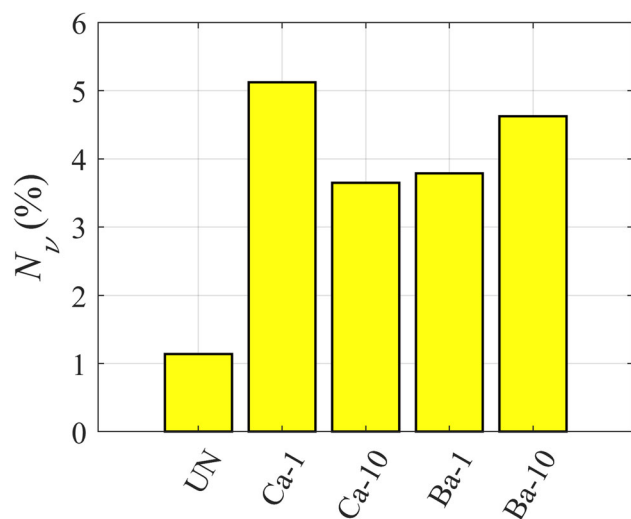
C. *Microparticle Number Density*

The 2D number densities, shown in Figure 7(a), demonstrate the challenge to distinguish the effect of microparticles numbers between the samples, especially UN and Ca. The difference in 3D number densities becomes significant, as seen in Figure 7(b). Although a slight loss of microparticles is observed, there is still no significant difference between UN, Ca-1, and Ca-10. The Ca-10 has ~ 2 pct fewer microparticles than Ca-1 and ~ 5 pct less than UN. These small losses alone cannot justify the 31 pct decrease in the graphite particle density from Ca-1 to Ca-10. Another possible explanation could be related to the Ostwald step rule,[43] where the microparticles are first formed in their metastable structures, which are more potent nuclei. A thermodynamic simulation showing this possibility is reported by Lekakh.[15] This explanation could also be extended to a potential inoculant interface or the degradation of potential carbon nanocrystals compounds reported by Qing *et al.*[14]

On the other hand, Ba-inoculated samples have very distinct behavior. Ba-1 has about 25 pct fewer microparticles than UN, while Ba-10 has a 14 pct increase in the microparticle population. This significantly lower number of microparticles is unclear. It could be related to the metastable liquid miscibility gap in the SiO_2–BaO system[44] or an increase in the flotation time of microparticles with higher density due to Ba addition.[15] For example, the density (g/mL) of BaO, BaS, and $BaO \cdot Al_2O_3 \cdot 2SiO_2$ are 5.72, 4.25, and 4.05, respectively. While the density (g/mL) of their calcium counterparts, *i.e.*, CaO, CaS, $CaO \cdot Al_2O_3 \cdot 2SiO_2$ are 3.35, 2.5, and 2.78, respectively.[45] The phases $CaO \cdot Al_2O_3 \cdot 2SiO_2$ and $BaO \cdot Al_2O_3 \cdot 2SiO_2$ are aluminosilicates proposed by Skaland *et al.*[4] No barium phases were not detected, indicating that their size or concentration is too small to be seen in the current SEM/EDX resolution. In a deoxidation study of steel using a Ba–ferrosilicon, Issagulov *et al.*[46] proposed that Ba-containing particles are absorbed by the slag phase more easily due to their smaller size.

In terms of microparticle types, the behavior of Ca and Ba samples are fundamentally different. While in Ca samples, the effect of holding time is seen in the loss of sulfides and gains of oxides and nitrides. For Ba samples, Ba-10 shows an increase in all populations compared to Ba-1, especially in the sulfides, which could be associated with the increase in the nucleation frequency.

When evaluating the area of the microparticle populations, shown in Figures 8(b) and (c), one can notice that inoculation increases the area of sulfides, oxides, and carbides. Ca-1 has a larger area occupied by sulfides and oxides, and these numbers decrease for Ca-10. The opposite is observed in the sulfide area for the Ba samples, which increases from Ba-1 to Ba-10. The oxide behavior of Ba samples is similar to Ca. Comparing the area with the 3D number densities, a decrease in the area and number density points to a loss of microparticles. This is mainly observed for sulfides in Ca samples.

Fig. 11—Nucleation potency for each sample.

In contrast, the Ba-10 sample increases the sulfide area and number density, pointing to a late formation and growth of new sulfides. This observation could be explained by: (i) slower reaction kinetics between (Ba, Ca, Al)–ferrosilicon and the melt, which might be the reason for improved performance with longer holding times in the Ba samples or/and (ii) flotation of microparticles due with higher density, explained above. The slow reaction kinetics for formation and phase transition for Ba-silicates compared with their Sr and Ca counterparts are known in the literature.[46,47]

V. CONCLUSIONS

The effect of inoculation and holding time in SGI specimens were studied using thermal analysis, microstructure evaluation, and SEM/EDX with AMICS for quantification of microparticles. The inoculants used were (Ca, Al)–FeSi and (Ba, Ca, Al)–FeSi.

The thermal analysis results showed that the undercooling, quantified using LET, is lower for all the inoculated samples, being highest for Ca samples. The LET value decreases with increasing holding time for all inoculated samples. It is estimated that Ca samples will reach the uninoculated undercooling in 11 minutes, while Ba samples in 48 minutes. The data clearly show a holding time resistance of SGI inoculated with (Ba, Ca, Al)–FeSi.

The microstructures showed that the uninoculated sample contains a mixture of Fe_3C and graphite in the structure. Ca-1 showed the highest nodule count density with 353 mm^{-2}, and a 5 minutes holding caused this number to decrease by 37 pct. The Ba samples started with a lower nodule count density of 225 mm^{-2}, but it increased with holding time.

AMICS coupled with an SEM/EDX was used to quantify the microparticles and the effect of holding time in their number densities. The microparticles were classified into sulfides, oxides, nitrides, and carbides. In the 2D measurements, no significant difference between the samples could be observed. The difference became apparent after using the FDM method to convert all the particles to 3D number densities. Inoculated samples have a higher graphite number density than UN. However, the difference in microparticle populations between UN and Ca samples could not fully explain the drop in nucleation potency that went from 5.1 to 3.5 pct after 10 minutes, which led to a decrease in the graphite nucleation between 31 and 37 pct. Therefore, other aspects related to the nucleation have to be considered, such as transients metastable states of interfaces or microparticles structures. On the other hand, there are significantly fewer microparticles in the Ba samples, which could be related to a miscibility gap in the oxide or sulfide system or flotation of microparticles. However, the number density and area of sulfides grow for Ba samples with increasing holding time, suggesting slower reaction kinetics of the Ba-containing inoculants forming late microparticles.

OPEN ACCESS

REFERENCES

1. D. Stefanescu: *ASM Handb.*, 2017, vol. 1, pp. 3–11.
2. D.M. Stefanescu: *Metals Handbook 10th Edition*, vol. 1, ASM International, Almere, 1990, pp. 3–11.
3. J. Lacaze: *Acta Mater.*, 1999, vol. 47, pp. 3779–92.
4. T. Skaland, Ø. Grong, and T. Grong: *Metall. Trans. A.*, 1993, vol. 24, pp. 2321–45.
5. D.M. Stefanescu, G. Alonso, and R. Suarez: *Metals.*, 2020, vol. 10, p. 221.
6. S.N. Lekakh: *Metall. Mater. Trans. B.*, 2019, vol. 50B, pp. 890–902.
7. M.N. Bhat, D.A. Khan, and K. Singh: *Int. J. Met. Cast.*, 2019, vol. 13, pp. 89–97.
8. I. Riposan and T. Skaland: in *Cast Iron Science and Technology Handbook*. D.M. Stefanescu, ed., American Society of Materials, Cleveland, 2017, pp. 160–76.
9. H. Nakae: *Int. J. Cast Met. Res.*, 2008, vol. 21, pp. 7–10.
10. A. Fay and P. Pinel: *Int. J. Met. Cast.*, 2020, vol. 14, pp. 1123–35.
11. G. Alonso, P. Larrañaga, D. Stefanescu, E. De la Fuente, A. Natxiondo, and R. Suarez: *Int. J. Met. Cast.*, 2017, vol. 11, pp. 14–26.
12. D. Stefanescu, A. Crisan, G. Alonso, P. Larrañaga, and R. Suarez: *Metall. Mater. Trans. A.*, 2019, vol. 50A, pp. 1763–72.
13. L. Laffont, A. Pugliara, T. Hungría, and J. Lacaze: *J. Mater. Res. Technol.*, 2020, https://doi.org/10.1016/j.jmrt.2020.02.093.

14. J. Qing, S. Lekakh, M. Xu, and D. Field: *Carbon.*, 2021, vol. 171, pp. 276–88.
15. S.N. Lekakh: *Int. J. Met. Cast.*, 2020, vol. 14, pp.1078-89.
16. L. Laffont, R. Jday, and J. Lacaze: *Metall. Mater. Trans. A.*, 2018, vol. 49A, pp. 1287–94.
17. J. Qing, V. Richards, and D.C. Van Aken: *Carbon.*, 2017, vol. 116, pp. 456–69.
18. M. Azeem, M. Bjerre, R. Atwood, N. Tiedje, and P. Lee: *Acta Mater.*, 2018, vol. 155, pp. 393–401.
19. C. Xu, T. Wigger, M.A. Azeem, T. Andriollo, S. Fæster, S. Clark, Z. Gong, R. Atwood, J.-C. Grivel, and J.H. Hattel: *Carbon*, 2021, https://doi.org/10.1016/j.carbon.2021.08.069.
20. E. Ghassemali, J.C. Hernando, D.M. Stefanescu, A. Dioszegi, A.E. Jarfors, J. Dluhoš, and M. Petrenec: *Scripta Mater.*, 2019, vol. 161, pp. 66–69.
21. T. Wigger, T. Andriollo, C. Xu, S. Clark, Z. Gong, R. Atwood, J. Hattel, N. Tiedje, P. Lee, and M. Azeem: *Acta Mater.*, 2021, vol. 221, p. 117367.
22. E. Fras and M. Górny: *Arch. Foundry Eng.*, 2008, vol. 8, p. 2008.
23. H. Head and S. Carolina: *1998 Keith D. Millis World Symposium on Ductile Iron*, American Foundrymen's Society, 1998, p. 313.
24. E. Huerta and V. Popovski: *Proc. AFS Cast Iron Inoculation Conf.*, 2005, pp. 29–30.
25. S.O. Olsen, T. Skaland, and C. Hartung: *66th World Foundry Congress*, 2004, pp. 891–902.
26. K.M. Pedersen and N.S. Tiedje: *Mater. Charact.*, 2008, vol. 59, pp. 1111–21.
27. X. Diao, Z. Ning, F. Cao, S. Ren, and J. Sun: *Mater. Sci. Technol.*, 2011, vol. 27, pp. 834–38.
28. Q. Tian, G. Wang, D. Shang, H. Lei, X. Yuan, Q. Wang, and J. Li: *Metall. Mater. Trans. B.*, 2018, vol. 49B, pp. 3137–50.
29. I.L.A. Daoud, N. Rimbert, A. Jardy, B. Oesterlé, S. Hans, and J.P. Bellot: *Adv. Eng. Mater.*, 2011, vol. 13, pp. 543–49.
30. D.M. Stefanescu: *AFS Cast Met. Res. J.*, 1973, pp. 8–13.
31. J. Takahashi and H. Suito: *Metall. Mater. Trans. A.*, 2003, vol. 34A, pp. 171–81.
32. C. Basak and A. Sengupta: *Scripta Mater.*, 2004, vol. 51, pp. 255–60.
33. D.M. Stefanescu: *ASM Handbook: Cast Iron Science and Technology*, vol. 1A, ASM International, Almere, 2017.
34. Y. Gulbin: *Image Anal. Stereol.*, 2008, vol. 27, pp. 163–74.
35. D.M. Stefanescu: *Int. J. Met. Cast.*, 2015, vol. 9, pp. 7–22.
36. V. Anjos, R. Deike, and C.S. Ribeiro: *Ciênc. Tecnol. Mater.*, 2017, vol. 29, pp. e27–33.
37. I. Riposan, S. Stan, V. Uta, and I. Stefan: *J. Mater. Eng. Perform.*, 2017, vol. 26, pp. 4217–26.
38. Y. Igarashi and S. Okada: *Int. J. Cast Met. Res.*, 1998, vol. 11, pp. 83–88.
39. J. Solberg and M. Onsøien: *Mater. Sci. Technol.*, 2001, vol. 17, pp. 1238–42.
40. J. Ekengård, A. Diószegi, and P.G. Jönsson: *Int. J. Met. Cast.*, 2016, vol. 10, pp. 500–15.
41. T. Quested and A. Greer: *Acta Mater.*, 2004, vol. 52, pp. 3859–68.
42. B. Domeij, J.C. Hernando, and A. Diószegi: *Metall. Mater. Trans. B.*, 2018, vol. 49B, pp. 2487–2504.
43. D. Turnbull: *Metall. Trans. B.*, 1981, vol. 12, pp. 217–30.
44. C.B. Carter and M.G. Norton: *Ceramic Materials: Science and Engineering*, Springer, Berlin, 2007.
45. H. Prophet: *JANAF Thermochemical Tables* (US Department of Commerce, Washington, 1985), *Cp Fitted by CRCT*, Montreal, 1971.
46. A. Issagulov, S.S. Kvon, V.Y. Kulikov, D. Aubakirov, and D. Issagulova: *Metalurgija.*, 2017, vol. 56, pp. 399–401.
47. M. Hyatt and N. Bansal: *J. Mater. Sci.*, 1996, vol. 31, pp. 172–84.